Electronic g-Tensors of Semiquinones in Photosynthetic Reaction Centers. A Density Functional Study

Sylwia Kacprzak and Martin Kaupp*

Institut für Anorganische Chemie, Universität Würzburg, Am Hubland, D 97074 Würzburg, Germany

Received: August 6, 2003; In Final Form: October 23, 2003

A recently developed density functional (DFT) approach for the calculation of electronic **g**-tensors has been applied to semiquinone radical anions in the different protein environments of photosynthetic reaction centers. Supermolecular models have been constructed, based on combined crystallographic and quantum chemical structure data, for the Q_A and Q_B active sites of bacterial reaction centers, for the A_1 site of photosystem I, as well as for ubisemiquinone in frozen 2-propanol. After scaling of the computed Δg_x components by 0.92, both Δg_x and Δg_y components computed at gradient-corrected DFT level with accurate spin−orbit operators agree with high-field EPR reference data essentially to within experimental accuracy in all four systems studied. The influence of the various semiquinone−protein noncovalent interactions has been studied by successive removal of individual residues from the models. The effects of hydrogen bonding to the two carbonyl oxygen atoms of the semiquinones are nonadditive, due to compensating spin-polarization effects. The effects of tryptophan−semiquinone π-stacking are different for Q_A and A_1 sites. This may be traced back to a different alignment of the interacting fragments and to differential spin polarization.

1. Introduction

Photosynthesis is the central biological process in which the energy of sunlight is converted into the biochemical energy essential to power life.[1] A wide variety of organisms is able to carry out photosynthesis. The crucial step of photosynthesis, in which the energy of electronic excitation is transformed to chemical redox energy, takes place in the reaction center (RC). The RC is an integral membrane pigment−protein complex incorporating many noncovalently associated cofactors which directly or indirectly take part in the electron transfer (ET) process. The charge separation taking place during ET leads to the formation of various radical pairs, several of which are ideally studied by electron paramagnetic resonance (EPR) spectroscopy. Among the most important bioradicals observed by EPR during the ET process are chlorophyll radical cations, pheophytin radical anions, and semiquinone radical anions.[1] It is the latter anions that we study here by quantum-chemical methods.

The information that may be extracted from EPR of bioradicals has recently been enhanced tremendously by the development of high-field EPR.[2] In particular, the electronic **g**-tensor may be resolved at higher magnetic fields and microwave frequencies. Importantly, the **g**-tensor has been shown to depend crucially not only on the type of semiquinone, but even more on the interactions of the semiquinone with the protein environment. This makes electronic **g**-tensors an important spectroscopic probe of semiquinone−protein interactions. An increasing number of high-field EPR experiments have now provided **g**-tensor information on semiquinones, either in frozen solution or in their natural protein environment.[3] Significant differences in the semiquinone **g**-tensors of different RCs have been found, due to environmental influences. For example, the **g**-tensor anisotropy of phyllosemiquinone (Vit-$K_1^{\bullet-}$) in the A_1 binding site of Photosystem I (PS-I) RC was found to be larger than one would expect (given the nature of the two semiquinones) from that of the ubisemiquinone ($UQ^{\bullet-}$) in the Q_A binding site of bacterial RCs (bRC). The **g**-anisotropy of the latter is in turn slightly larger than that for the same semiquinone in the Q_B binding site of bRCs.[4−9] These differences are thought to be mainly due to different noncovalent interactions with the protein environment. The main interactions are hydrogen bonds to the carbonyl oxygen atoms of the semiquinone, but π- or T-stacking interactions are also at the focus of current research.[10] As the same interactions influence also the redox potentials of the quinone/semiquinone redox couples and thus their function in the ET, detailed insight into the interrelations between **g**-tensor and environment is of considerable interest.

Quantum chemical calculations may provide central information about these interrelations. While semiempirical methods have provided important qualitative insights into the **g**-tensors of semiquinone radical anions,[11] quantitative treatments became possible only recently, in particular by using density functional theory (DFT). In a recent systematic DFT study of various semiquinones, quantitative agreement with experimental Δg_x components measured in frozen 2-propanol has been achieved after scaling by a factor of 0.92, whereas the Δg_y components were reproduced within experimental accuracy without scaling.[12] To achieve this accuracy, hydrogen bonding to solvent molecules, as well as the conformational arrangement of the substituents of the semiquinones, had to be taken into account accurately[12] (see refs 13 and 14 for further DFT and MCSCF studies of **g**-tensors for semiquinone radical anions). The same DFT method[15] was then applied to understand interactions between tryptophan (Trp) and quinones/semiquinones in the A_1 binding site of PS-I.[10] It was shown that the unusually large Δg_x and Δg_y values measured in reaction centers reconstituted with smaller quinones[16] may be explained by novel T-stacking H-bonding interactions between the Trp N−H function and the π-system of the semiquinone. This may have appreciable

* Correspondence author. E-mail: kaupp@mail.uni-wuerzburg.de. Fax: ++49 931 888 7135.

10.1021/jp036322h CCC: $27.50
Published on Web 01/22/2004

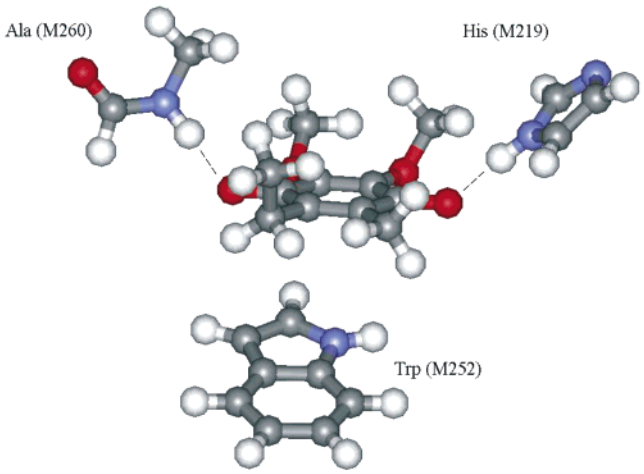

Figure 1. Model of the Q_A binding site of bRC, with UQ-EM$^{\bullet-}$, nmf, histidine, and indole.

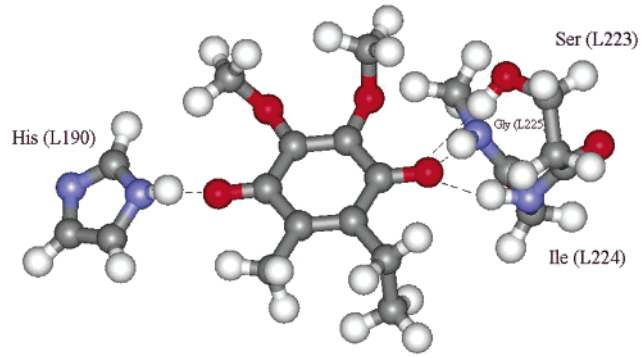

Figure 2. Model of the Q_B binding site of bRC, with UQ-EM$^{\bullet-}$, histidine, and SIG-fragment.

consequences for the role of Trp residues in the neighborhood of quinones in biological systems.[10]

Here we use the same DFT approach[12,15] to study the **g**-tensors of a wider set of semiquinone active sites of photosynthetic RCs. The purpose of this study is 2-fold: (a) to confirm the predictive power of the method found for in vitro systems also for a number of realistic models from protein environments and (b) to analyze in detail the influence of the various semiquinone−protein interactions on the computed **g**-tensors. The study concentrates on models for three distinct active sites of RCs, for which high-resolution X-ray structures are available:[17,18] the A_1 phylloquinone binding site of PS-I and both Q_A and Q_B ubiquinone binding sites of bRC. In addition, we include models for ubisemiquinone in frozen 2-propanol, in extension of the study in ref 12. We carry out calculations for realistic models of the entire active site, as well as for systems that include only a subset of the semiquinone−protein interactions. Together with further analysis tools, this is expected to shed light on the influence of specific residues on the **g**-tensor.

2. Computational Details

Structures. The models for ubisemiquinone in the Q_A and Q_B sites (see Figures 1 and 2, respectively) were based on the 2.6 Å resolution X-ray structure obtained for *Rhodobacter (Rb.) sphaeroides* in the charge-separated $P^+Q_B^{\bullet-}$ state.[17] Three residues interact strongly with UQ$^{\bullet-}$ in the Q_A binding site (Ala M260, His M219, Trp M252), among which Ala M260 and His M219 H-bond to the two semiquinone carbonyl oxygen atoms, whereas Trp M252 exhibits a moderate π-stacking interaction with UQ$^{\bullet-}$. In our model, Ala M260 was substituted by an nmf (*N*-methylformamide) molecule, His M219 by imidazole, and Trp M252 by indole. The isoprenoid side chain of UQ$^{\bullet-}$ is not expected to influence the **g**-tensor appreciably[12] and was replaced either by a methyl or an ethyl group. The same substitution was applied to all other models. Overall, the model for Q_A consisted of the semiquinone UQ-M$^{\bullet-}$ or UQ-EM$^{\bullet-}$ [2,3-dimethoxy-5,6-dimethyl or 5-ethyl-6-methyl-1,4-benzoquinone, respectively], nmf, imidazole, and indole (Figure 1).

Four amino acid residues (His L190, Ser L223, Ile L224, Gly L225) have been included in our model of the Q_B binding site, all of which participate in hydrogen bonding to the two semiquinone carbonyl oxygen atoms. His L190 was modeled by imidazole. The part of the protein backbone consisting of Ser L223, Ile L224, and Gly L225 (SIG fragment) was directly cut out of the crystallographically determined structure and terminated by hydrogen atoms as follows: the amino group of Ser, the carbonyl group of Gly, and the hydrocarbon side chain of the Ile were each replaced by hydrogen (Figure 2). In view of the flexibility of the Q_B site, we regard it as essential that intermolecular parameters could be extracted from the charge-separated $P^+Q_B^{\bullet-}$ state. As this should provide more realistic hydrogen bonding, we chose this 2.6 Å resolution structure[17] over available "ground-state structures" at higher resolution. Note that a recent 3.0 Å resolution structure of the $P^+Q_A^{\bullet-}$ state indicated no structural changes in the Q_A site relative to the $P^+Q_B^{\bullet-}$ state,[19] and therefore we regard it as appropriate to use the data for this state also as a starting point for our model of the Q_A site (see above). Note that, in addition to the X-ray data, EPR and ENDOR have provided further evidence for the presence or absence of semiquinone−protein interactions in these sites.[3,20] In the present study we neglect the potential influence of the iron atom that is located between the Q_A and Q_B sites, coordinated to His M219 on the Q_A side and to His L190 on the Q_B side. We cannot exclude completely the possibility that this center (or the zinc atom by which iron is often replaced to obtain simplified EPR spectra) might provide a small additional influence on the **g**-tensors of the semiquinones in both sites. This could be either by direct electrostatic effects or by an indirect slight polarization of the hydrogen bonds from histidine to the corresponding semiquinone. These potential influences will be the subject of further studies.

Our model for the A_1 binding site of PS-I is based on the 2.5 Å resolution X-ray structure for the cyanobacterium *Synechococcus elongatus*.[18] The relevant interactions include phyllosemiquinone (Vit-$K_1^{\bullet-}$) and two amino acid residues (Leu A722 and Trp A697). Vit-$K_1^{\bullet-}$ was modeled by DMNQ$^{\bullet-}$ or EMNQ$^{\bullet-}$ (2,3-dimethyl- or 2-ethyl-3-methyl-1,4-naphthosemiquinone), Leu A722 was substituted by nmf, and Trp A697 by indole (see Figure 3). Again, the choice of interacting residues is consistent with further EPR and ENDOR data, and also with recent mutation studies that indicate negligible spectroscopic changes upon modification of a nearby hydrogen bonding network that includes residues Tyr A696, Ser A692, and Met A688.[21]

To reproduce the **g**-tensors accurately, it was mandatory to account properly for hydrogen bonding to the carbonyl oxygen atoms, as well as for the conformational arrangement of the substituents of the semiquinone. We kept intermolecular structure parameters, as well as the dihedral angles of the methoxy substituents in UQ$^{\bullet-}$, at their crystallographic values. However, in view of the limited accuracy of the protein crystallographic data, all other intramolecular parameters were substituted by values obtained from full DFT optimizations performed for each

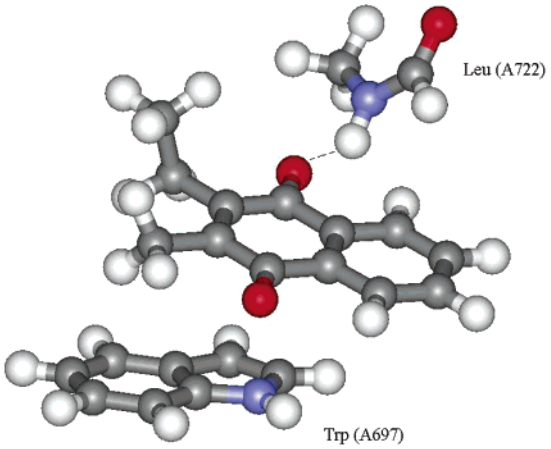

Figure 3. Model of the A_1 binding site of Photosystem I, with $EMNQ^{\bullet-}$, nmf, and indole.

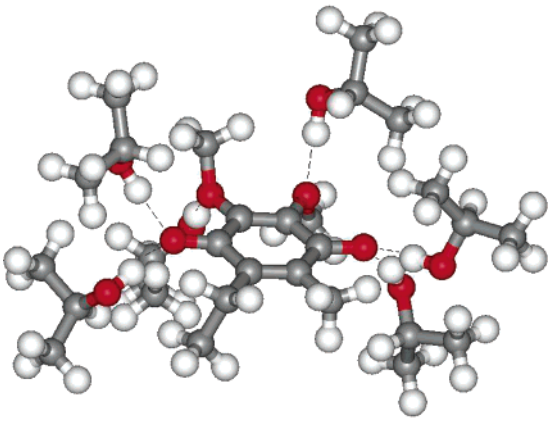

Figure 4. UQ-$EM^{\bullet-}$(2-PrOH)$_6$ model of ubisemiquinone in frozen 2-propanol solution.

individual component of the models. The optimizations were carried out at the gradient-corrected DFT level (BP86 functional[22,23]), with the Gaussian 98 program.[24] As in our previous studies,[10,12] effective-core potentials (ECPs) and DZP valence basis sets were used for C, O, and N,[25] and a DZV basis set for hydrogen.[26] As the crystallographic data files contain only information about the positions of heavy atoms, most hydrogen atom positions were fully optimized for a given fragment. The available information on hydrogen bond lengths from ENDOR data is not very accurate.[3a] Therefore, the positions of most hydrogen atoms participating in hydrogen bonds (with the exception of the SIG fragment in the Q_B site, see above) were obtained by restricted optimizations of bimolecular complexes of the semiquinone with the corresponding hydrogen bond donor, keeping all further inter- and intramolecular structural parameters constant. The following hydrogen bond lengths have been obtained and were employed in the **g**-tensor calculations. Q_A site: UQ-$EM^{\bullet-}$−nmf 1.82 Å, UQ-$EM^{\bullet-}$−imidazole 1.78 Å. Q_B site: UQ-$EM^{\bullet-}$−imidazole 1.81 Å, UQ-$EM^{\bullet-}$−SIG 2.24 Å (Ser L223), 1.98 Å (Ile L224), and 2.39 Å (Gly L225).[27] A_1 site: $EMNQ^{\bullet-}$−nmf 1.85 Å. These values agree reasonably well with spectroscopic estimates.[3a]

To model $UQ^{\bullet-}$ in frozen 2-propanol, the fully DFT-optimized structures of dimethyl-substituted model complexes [UQ-$M^{\bullet-}$(2-PrOH)$_6$ or UQ-$M^{\bullet-}$(2-PrOH)$_4$] were taken from ref 12. In addition, the corresponding complexes with UQ-$EM^{\bullet-}$ were also fully optimized at the BP86/DZP level (see, e.g., Figure 4). The optimized hydrogen bond lengths were 1.74−1.78 Å for the four H-bonds to the carbonyl oxygen atoms and 1.80 Å for the two H-bonds to the methoxy substituents.

g-Tensor Calculations. All details of the **g**-tensor calculations were as described in ref 12. Here we only summarize the main features. The calculations used the deMon program[28] and the associated **g**-tensor module.[15] The uncoupled DFT level was employed, with the BP86 functional[22,23] and DZVP basis sets.[26] As has been shown previously,[12,15] the modest DZVP basis set provides a good compromise between accuracy and computational effort. The one- and two-electron spin−orbit (SO) operators were treated by the accurate and efficient all-electron atomic meanfield approximation (AMFI),[29,30] which has the main advantage of covering the important spin−other orbit contributions.[15,31] The common gauge origin for the magnetic vector potential was chosen to be at the midpoint between the two carbonyl oxygen atoms. This is justified by previous experience, and by the overall low gauge dependence of the **g**-tensor components (compared to, e.g., the NMR chemical shift tensor). In our calculations, the **g**-tensor is defined as $\mathbf{g} = g_e(\mathbf{1}) + \Delta\boldsymbol{g}$, where $g_e = 2.002319$. In the following we present and discuss g-shift (Δg) values defined as a correction to the free-electron value in ppm (that is, in units of 10^{-6}). Note that our approach includes not only the second-order spin−orbit/orbital-Zeeman terms but also the relativistic mass correction (RMC) and the one-electron part of the gauge correction (GC) terms.[15]

The calculations in this work are on supermolecular model complexes that account for the direct interactions of the semiquinone with the neighboring amino acid residues, whereas further long-range electrostatic contributions are neglected. We have recently evaluated the use of continuum solvent models in **g**-tensor calculations.[32] We noted that, after accounting for explicit H-bond interactions in protic solvents using supermolecular models, the continuum solvent model made only very small further contributions to the **g**-tensor. This was even the case when the dielectric constant for water of $\epsilon = 78.39$ was employed.[32] Given the much smaller dielectric constants of $\epsilon \approx 4$ that are usually considered for proteins, we do not expect major effects of continuum solvent models when added to our supermolecular systems. Obviously, these considerations do not apply to charged residues, where generally more important long-range effects might be expected (see discussion above). A consideration of dynamical effects on the **g**-tensor is outside the scope of this study but these are currently investigated by ab initio molecular dynamics simulations for semiquinones in aqueous solution.[33]

3. Results and Discussion

The computed g-shift components of the investigated model complexes are collected in Table 1, which includes also the experimental high-field EPR reference values. In the following, we will focus mostly on the most characteristic Δg_x component (parallel to the carbonyl C−O vectors), which depends particularly on the environment. We will also point out specific features in Δg_y (in-plane but perpendicular to the C−O vectors). The Δg_z component (out-of-plane) cannot be discussed meaningfully, as it is too small (and dominated by diamagnetic contributions). Note that in all cases studied here, the orientation of the tensor deviates by less than 5°, but usually even by less than 2°, from ideal alignment with the semiquinone framework.

As was found in our comparison between computed and experimental values for a series of semiquinones in frozen 2-propanol,[10,12] deficiencies in the currently available state-of-the-art gradient-corrected density functionals cause a systematic overestimate of Δg_x by ca. 8−10%. This may be corrected via

TABLE 1: Computed and Experimental *g*-Shift Components (in ppm) for Semiquinone Radical Anions with a Breakdown of Active-Site Models into their Constituent Contributions

model	Δg_x[g]		Δg_y	Δg_z
exp $Q_A^{\bullet-}$ in Zn-bRCs[a]	**4300**		**3100**	**−100**
exp $Q_A^{\bullet-}$ in Zn-bRCs[b]	**4170**		**3000**	**−220**
UQ-$M^{\bullet-}$ (imidazole−nmf−indole)	4659	(4286)	3061	12
UQ-$EM^{\bullet-}$(imidazole−nmf−indole)	4730	(4352)	3052	11
UQ-$EM^{\bullet-}$(nmf−indole)	5070	(4664)	3153	23
UQ-$EM^{\bullet-}$(imidazole−indole)	5171	(4757)	3136	7
UQ-$EM^{\bullet-}$(indole)	5439	(5224)	3301	24
UQ-$EM^{\bullet-}$(imidazole−nmf)	4629	(4259)	2998	−61
UQ-$EM^{\bullet-}$(nmf)	4983	(4584)	3120	−43
UQ-$EM^{\bullet-}$(imidazole)	5053	(4649)	3110	−16
UQ-$EM^{\bullet-}$	5298	(4874)	3243	−5
exp UQ-$10^{\bullet-}$ in 2-PrOH[c]	**4140**		**3100**	**−100**
exp UQ-$3^{\bullet-}$ in 2-PrOH[d]	**3900**		**2940**	**−220**
UQ-$M^{\bullet-}$(2-PrOH)$_6$	4425	(4071)	2944	20
UQ-$EM^{\bullet-}$(2-PrOH)$_4$	4269	(3927)	2880	47
UQ-$EM^{\bullet-}$(2-PrOH)$_6$	4393	(4042)	2927	70
UQ-$EM^{\bullet-}$	5853	(5385)	3325	1
exp $Q_B^{\bullet-}$ in Zn-bRCs[b]	**3940**		**2950**	**−190**
UQ-$M^{\bullet-}$ (imidazole−SIG)	4202	(3866)	2902	−68
UQ-$EM^{\bullet-}$(imidazole−SIG)	4254	(3914)	2874	−68
UQ-$EM^{\bullet-}$(SIG)	4716	(4339)	3014	−60
UQ-$EM^{\bullet-}$(imidazole)	5004	(4604)	3110	−41
UQ-$EM^{\bullet-}$	5251	(4831)	3234	−30
exp $A_1^{\bullet-}$ in PS-I[e]	**3900**		**2750**	**−140**
DMN$Q^{\bullet-}$(indole−nmf)	4082	(3755)	2699	−12
DMN$Q^{\bullet-}$(indole−nmf), MP2[f]	4227	(3889)	2707	14
EMN$Q^{\bullet-}$(indole−nmf)	4129	(3799)	2683	−9
EMN$Q^{\bullet-}$(indole)	4458	(4101)	2785	32
EMN$Q^{\bullet-}$(nmf)	4219	(3881)	2679	36
EMN$Q^{\bullet-}$	4548	(4184)	2791	−5

[a] W-band EPR for zinc-substituted bRC.[4] [b] Q-band EPR in zinc-substituted bRC of *Rb. sphaeroides* R-26, with fully deuterated UQ-$10^{\bullet-}$.[9] [c] W-band EPR in frozen 2-propanol.[4,5] [d] Q-band EPR in 2-propanol-d_8 (Nimz, O.; Lendzian, F.; Lubitz, W. *Appl. Magn. Reson.* **1998**, *14*, 255). [e] Transient spin-polarized W-band EPR on $P_{700}^{\bullet+}A_1^{\bullet-}$ in a PS-I single crystal.[6] [f] MP2-optimized structure employed, cf. ref 10. [g] Values in parentheses have been scaled by 0.92 (cf. ref 12).

scaling by 0.92.[12,34] After scaling (values in parentheses in Table 1), the computed Δg_x results for the best (complete) models agree remarkably well with experiment in all four cases studied here. Maximum deviations from experiment are typically in the range of ca. ±100 ppm, which has also been reported as the typical experimental uncertainty in current high-field EPR experiments.[4,5] As found for the previously studied in vitro systems,[12] results for Δg_y are generally within these limits without any scaling.[34] In the following discussion, we will use the scaled Δg_x and unscaled Δg_y values. Table 1 also provides previous results[10] for the DMN$Q^{\bullet-}$(indole−nmf) model of the A_1 site. The Δg_x component is about 100 ppm larger in these calculations than in the present work, due to the fact that MP2- rather than DFT-optimized fragment structures were employed (MP2 optimizations were used consistently in ref 10, to account for dispersion contributions to π-stacking interactions, in particular for neutral quinone−indole complexes). We note in passing that differences between methyl- and ethyl-substituted model semiquinones are rather small (the largest difference is 66 ppm for Δg_x in the Q_A site).

The computed results for the isolated semiquinones (Δg_x = 4184 ppm for EMN$Q^{\bullet-}$ and $\Delta g_x \approx$ 4800 ppm for UQ-$EM^{\bullet-}$) show that part of the difference between observed *g*-anisotropies for the PS-I and bRC active sites arises from the intrinsic properties of the semiquinone (see also refs 11 and 12 for analyses). Large effects of methoxy group conformations in ubisemiquinone models on *g*-shifts have already been identified in ref 12. In our models, both angles and dihedral angles defining the conformations of the methoxy substituents were taken unchanged from the X-ray structure files. The small difference in the Δg_x values (43 ppm) for isolated UQ-$EM^{\bullet-}$ in the $Q_A^{\bullet-}$ and $Q_B^{\bullet-}$ models reflects slight differences in the out-of-plane dihedral angles and bond angles of the methoxy substituents (see also below).

While the intrinsic properties of the semiquinone contribute to the differences between the A_1 site of PS-I and the bacterial reaction centers, it is mainly the environmental interactions that modify the Δg_x values for the different ubisemiquinone-based systems. As is well-known, the decisive influence is hydrogen bonding to the carbonyl oxygen atoms. This reduces Δg_y to some extent, but in particular Δg_x is reduced noticeably (Table 1). In the A_1 binding site model, the single hydrogen bond to nmf (model for Leu A722) reduces Δg_x of isolated EMN$Q^{\bullet-}$ by 303 ppm (7%). The two hydrogen bonds (models for Ala M260, His M219) in the Q_A binding site of bRC decrease Δg_x of isolated UQ-$EM^{\bullet-}$ by 615 ppm (13%), whereas in the Q_B binding site the reduction is 917 ppm (19%), due to four hydrogen bonds of variable orientation and strength (models for His L190, Ser L223, Ile L224, Gly L225). Interestingly, the effect of four H-bonds in the Q_B site is not twice larger than that of two H-bonds in the Q_A site, probably due to the fact that some of the bonds in the Q_B site are noticeably longer than the H-bonds to Ala M260 and His M219 in the Q_A site. As discussed further below, the effects of different hydrogen bonds do not necessarily have to be additive.

Experimentally, both Δg_x and Δg_y in the Q_B site are somewhat lower than in the Q_A site. This is well reproduced by the calculations and reflects the more pronounced hydrogen bonding in the Q_B site, which is furthermore known to be open to the cytoplasm via a hydrophilic channel.[1] Interestingly, the calculations suggest that both Δg_x and Δg_y in the models for UQ-$10^{\bullet-}$ in 2-propanol are intermediate between the Q_A and Q_B results (experimental results for UQ-$10^{\bullet-}$ agree with this notion, whereas the values for UQ-$3^{\bullet-}$ are lower). As may be seen clearly from the comparison of results for UQ-$EM^{\bullet-}$(2-PrOH)$_4$ and UQ-$EM^{\bullet-}$(2-PrOH)$_6$, this is in part due to the extra hydrogen bonds to the methoxy substituents of ubisemiquinone. These additional interactions, which are apparently absent in the two protein environments, have been shown previously to increase both Δg_x and Δg_y.[12]

In addition, comparison of the free ubisemiquinones reveals a significantly larger Δg_x (by more than 500 ppm) and a somewhat larger Δg_y (by ca. 100 ppm) for UQ-$EM^{\bullet-}$ when taken from the optimized UQ-$EM^{\bullet-}$(2-PrOH)$_6$ structure rather than from the Q_A or Q_B models. This must reflect the different methoxy-group conformations. Our previous analyses showed[12] that dihedral angles between 40° and 60° (as found for optimized isolated ubisemiquinone models) provide particularly low Δg_x and Δg_y values, whereas maximal values are obtained in the range between 90° and 120° (dihedral angles found for solvated supermolecular models[12]). Closer inspection of the methoxy out-of-plane dihedral angles in the systems of interest in this study provides interesting insights: the two methoxy out-of-plane angles in the UQ-$EM^{\bullet-}$(2-PrOH)$_6$ system are 92.0° and 98.7°, i.e., both in the range of maximal Δg_x and Δg_y. In contrast, in the Q_A site, the dihedral angles are ca. 72.5° for the methoxy group closer to the hydrogen bond with His M260, and 125.6° for that close to the H-bond with Ala M219 (Figure 1). In particular the former dihedral angle is already in a range that will lead to lower Δg_x and Δg_y. Inspection of the bRC X-ray

data[17] indicates much higher steric demand of the protein backbone near Ala M219 than near His M260. We presume that this forces the lower dihedral angle of the methoxy group near His M260 and thus the lower Δg_x and Δg_y values compared to UQ-EM$^{\bullet-}$ in the conformation of the UQ-EM$^{\bullet-}$(2-PrOH)$_6$ model. Similarly, in the Q_B site, the steric demand of the backbone near the Ser L223, Ile L224, and Gly L225 residues (SIG fragment in the model, cf. Figure 2) forces a larger dihedral angle of 99.7°, whereas His L190 hydrogen bonds from the side of the semiquinone opposite the methoxy groups and thus allows a very small dihedral angle of 61.2° for the closest methoxy substituent. Part of this lowering of the Δg_x and Δg_y values for the isolated semiquinones in the structures derived from Q_A and Q_B compared to the UQ-EM$^{\bullet-}$(2-PrOH)$_6$ model survives in the full supermolecular models, i.e., when the environmental effects are taken into account. Together with the extra hydrogen bonds to the methoxy oxygen atoms in solution (see above) these conformational effects explain the relatively low values found experimentally for the protein environment compared to 2-propanol solution (Table 1), despite the more extensive hydrogen bonding in the latter environment. Note that the conformation of the methoxy substituents is thought to influence also the redox potential of the quinone/semiquinone pair.[3a,35]

As we noted previously,[12] the reduction of Δg_x by simultaneous hydrogen bonds to both carbonyl oxygens is more pronounced than the sum of the individual effects of hydrogen bonding to each carbonyl oxygen separately. The same lack of additivity is apparent for both the Q_A and Q_B models. While in the Q_A models the sum of individual reductions of Δg_x from isolated UQ-EM$^{\bullet-}$ by nmf and imidazole is calculated to be −415 ppm, the total effect of both hydrogen bonds is computed to be −615 ppm. Similarly, the reduction of Δg_x by the sum of individual contributions from the imidazole and SIG fragments in the Q_B model is −719 ppm, but the total reduction is computed to be −917 ppm. Closer analysis of the nonadditivity showed[12] that in the case of asymmetric H-bonding the spin density is polarized in the direction of the noncoordinated carbonyl oxygen. The reduced spin−orbit contributions to the **g**-tensor from the coordinated oxygen are thus partly compensated by an enhancement of SO effects from the noncoordinated oxygen.[12] This compensation by spin polarization ceases to work when H-bonds exist to both carbonyl oxygen atoms. Spin polarization effects should bear also on the model for the A_1 site, where only one of the carbonyl oxygen atoms is involved in hydrogen bonding. This is expected to keep the reduction of Δg_x by H-bonding small in this case. The polarization of spin density by unsymmetrical hydrogen bonding is also apparent in experimental and computed β-hydrogen hyperfine coupling constants.[36]

In the Q_A and A_1 binding sites, further noncovalent interactions arise from π-stacking of the semiquinone with a nearby Trp residue, which has been modeled here by an indole molecule, as in ref 10. The effect of this π-stacking on the **g**-tensor is moderate but nonnegligible (see also ref 10), and it appears to be rather different for the Q_A and A_1 models. In the A_1 model, the effect is small on Δg_x (ca. −80 ppm) and negligible on Δg_y. In contrast, both Δg_x and Δg_y are *increased* in the Q_A models. In this case, strong nonadditivity is found for Δg_x: while a significant effect of +350 ppm is predicted when indole is added to isolated UQ-EM$^{\bullet-}$, the effect is only +93 ppm when the indole is added in the presence of the two hydrogen bonds. Apparently, the presence of hydrogen bonding reduces the influence of π-stacking on Δg_x.

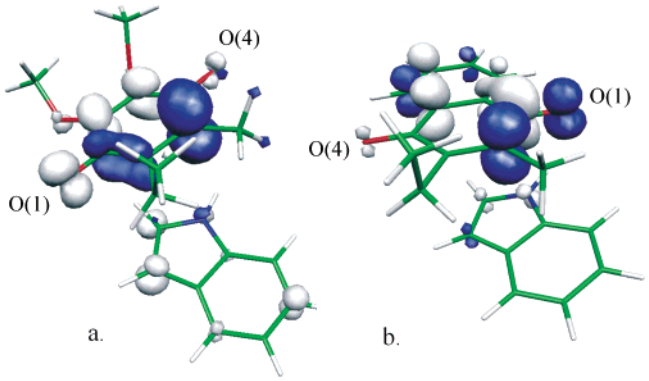

Figure 5. Plots of differences in spin density ($\pm 10^{-4}$ au) with and without an indole π-stacked to the semiquinone. Blue isosurfaces indicate a reduction of spin density, gray ones indicate an enhancement due to the intermolecular interactions. (a) UQ-EM$^{\bullet-}$(indole) from the Q_A site of bRC; (b) EMNQ$^{\bullet-}$(indole) from the A_1 site of PS-I.

The effect of π-stacking with a nearby Trp residue seems thus to be slightly more pronounced and in the opposite direction in the Q_A site compared to the A_1 site, although the average π-stacking distance is larger (4.1 Å in Q_A vs 3.4 Å in A_1). These differences appear to be related to the relative arrangements of semiquinone and indole molecules (Figures 1 and 3). In the A_1 model they are aligned nearly parallel, with the pyrrole ring of indole eclipsed by the benzosemiquinone ring of EMNQ$^{\bullet-}$. This allows genuine $\pi-\pi$ interactions. In the Q_A model, the indole molecule is not only shifted to a side of semiquinone but is also tilted slightly from the parallel alignment (∼15°), thus reducing $\pi-\pi$ interactions but potentially enhancing electrostatic polarization effects. The different relative alignment in the two systems results in different polarization of spin densities (Figure 5), the net effect of which actually turns out to be larger for Q_A than for A_1. In the case of the UQ-EM$^{\bullet-}$−indole bimolecular model complex for Q_A, the intermolecular interaction moderately increases the spin density on both semiquinone carbonyl oxygen atoms in an asymmetric fashion (Figure 5a). In contrast, in the EMNQ$^{\bullet-}$−indole model for A_1, the spin density on one carbonyl oxygen O(4) is increased slightly, but that on the other oxygen atom O(1) is reduced much more (Figure 5b). As oxygen spin−orbit coupling is mainly responsible for the *g*-shifts,[12] an overall increase/decrease of spin-density on the carbonyl oxygens will enhance/reduce the Δg_x component (the Δg_y component is affected much less). It should be noted that a recent computational study suggested the π-interactions between semiquinones and indole to be repulsive, or at least inferior to other arrangements, whereas they are clearly attractive for the neutral quinone.[10] In the anionic systems, the computations strongly favored a T-stacking arrangement. This should be kept in mind when we discuss the π-stacking based on the X-ray structure obtained for the neutral quinone.

In view of the rather different **g**-tensors computed for isolated (gas-phase) EMNQ$^{\bullet-}$ and UQ-EM$^{\bullet-}$ radicals (Table 1), the overall Δg_x components in the A_1 and Q_B sites are remarkably similar. Obviously, the intrinsically lower Δg_x of EMNQ$^{\bullet-}$ is compensated by the stronger H-bonding to UQ-EM$^{\bullet-}$ in the Q_B site.

A similar breakdown of the individual environmental contributions to the **g**-tensor of Vit-$K_1^{\bullet-}$ in the A_1 site has been attempted recently.[13] Unfortunately, neither the computational methods nor the structural models employed were adequate for a precise analysis. The two-component ZORA method employed neglects spin polarization (as well as spin−other-orbit contributions) and overestimates Δg_x and Δg_y considerably. The

environmental effects, which were computed to be much larger than we find here, are therefore probably severely overestimated.

4. Conclusions

The density functional approach of ref 15 reproduces experimental **g**-tensors for semiquinones remarkably well in a variety of protein environments, as well as for frozen protic solution, provided that the Δg_x component is scaled by a factor of 0.92 to account for systematic deficiencies of the currently used density functionals.[12,15,34] We believe that these types of DFT calculations are a valuable tool to augment experimental studies of bioradicals, and the computations provide both quantitative predictive power and qualitative insights. A recent application to PS-I is a good further example.[10]

The supermolecular models for the binding sites have been decomposed to analyze the influence of specific semiquinone−protein interactions in detail. The effects of hydrogen-bonding interactions are nonadditive, due to compensating effects of spin polarization in unsymmetrically H-bonded systems. In addition, π-stacking with nearby Trp residues provides further moderate contributions to the **g**-tensor, which are notably different for the Q_A site of bacterial reaction centers and the A_1 site of PS-I. These differences have been traced back to the different alignment of Trp relative to the semiquinone in the two systems, leading to different spin-polarization contributions. Last but not least, in ubisemiquinone model systems the conformations of the methoxy substituents (and H-bonding to the methoxy-oxygen atoms) have important influences on the **g**-tensor[12] and need to be considered in a full interpretation of EPR data.

Acknowledgment. This study has been supported by Deutsche Forschungsgemeinschaft (Priority Program SP1051, "High-Field EPR") and by Fonds der Chemischen Industrie. Part of this work benefitted also from the graduate college "Moderne Methoden der magnetischen Resonanz in der Materialforschung" at Universität Stuttgart.

Supporting Information Available: Tables S1−S4 containing Cartesian coordinates of the supermolecular models employed in the **g**-tensor calculations. This material is available free of charge via the Internet at http://pubs.acs.org.

References and Notes

(1) Blankenship, R. E. *Molecular Mechanisms of Photosynthesis*; Blackwell Science: Oxford, UK, 2002.

(2) For reviews see, e.g.: Möbius, K. *Biological Magnetic Resonance*; Berliner, L. J., Reuben, J., Eds.; Plenum Press: New York, 1993; Vol. 13, pp 253−274. Prisner, T. F. *Advances in Magnetic and Optical Resonance*; Warren, W., Ed.; Academic Press: New York, 1997; Vol. 20, pp 245−299 and references therein.

(3) See, e.g.: (a) Lubitz, W.; Feher, G. *Appl. Magn. Reson.* **1999,** *17*, 1. (b) Levanon, H.; Möbius, K. *Annu. Rev. Biophys. Biomol. Struct.* **1997,** *26*, 495.

(4) Burghaus, O.; Plato, M.; Rohrer, M.; Möbius, K.; MacMillian, F.; Lubitz, W. *J. Phys. Chem.* **1993**, *97*, 7639.

(5) Rohrer, M.; Plato, M.; MacMillan, F.; Grishin, Y.; Lubitz, W.; Möbius, K. *J. Magn. Reson.* **1995,** *116*, 59.

(6) Zech, S. G.; Hofbauer, W.; Kamlowski, A.; Fromme, P.; Stehlik, D.; Lubitz, W.; Bittl, R. *J. Phys. Chem. B* **2000**, *104*, 9728.

(7) van der Est, A.; Prisner, T. F.; Bittl, R.; Fromme, P.; Lubitz, W.; Möbius, K.; Stehlik, D. *J. Phys. Chem. B* **1997,** *101*, 1437.

(8) MacMillan, F.; Hanley, J.; van der Weerd, L. J.; Knüpling, M.; Un, S.; Rutherford, A. W. *Biochemistry* **1997,** *36*, 9297.

(9) Isaacson, R. A.; Lendzian, F.; Abresch, E. C.; Lubitz, W.; Feher, G. *Biophys. J.* **1995**, *69*, 311.

(10) Kaupp, M. *Biochemistry* **2002,** *41*, 2895.

(11) See, e.g.: Knüpling, M.; Törring, J. T.; Un, S. *Chem. Phys.* **1996,** *219*, 291. Törring, J. T.; Un, S.; Knüpling, M.; Plato, M.; Möbius, K. *J. Chem. Phys.* **1997,** *107*, 3905.

(12) Kaupp, M.; Remenyi, C.; Vaara, J.; Malkina, O. L.; Malkin, V. G. *J. Am. Chem. Soc.* **2002,** *124*, 2709.

(13) Teutloff, C.; Hofbauer, W.; Zech, S. G.; Stein, M.; Bittl, R.; Lubitz, W. *Appl. Magn. Reson.* **2001,** *21*, 363.

(14) Neyman, K. M.; Ganyushin, D. I.; Rinkevičius, Ž.; Rösch, N. *Int. J. Quantum Chem.* **2002,** *90*, 1404. Engström, M.; Vahtras, O.; Ågren, H. *Chem. Phys.* **1999,** *243*, 263.

(15) Malkina, O. L.; Vaara, J.; Schimmelpfennig, B.; Munzarova, M.; Malkin, V. G.; Kaupp, M. *J. Am. Chem. Soc.* **2000,** *122*, 9206.

(16) Sieckmann, I.; van der Est, A.; Bottin, H.; Sétif, P.; Stehlik, D. *FEBS Lett.* **1991**, *98*, 284. van der Est, A.; Sieckmann, I.; Lubitz, W.; Stehlik, D. *Chem. Phys.* **1995**, *349*, 194.

(17) Stowell, M. H.; McPhillips, T. M.; Rees, D. C.; Soltis, S. M.; Abresch, E.; Feher, G. *Science* **1997**, *276*, 812.

(18) Jordan, P.; Fromme, P.; Witt, H. T.; Klukas, O.; Saenger, W.; Krauss, N. *Nature* **2001**, *411*, 909.

(19) See results quoted in ref 3a.

(20) See, e.g.: Deligiannakis, Y.; Rutherford, A. W. *BBA-Bioenerget.* **2001**, *1507*, 226.

(21) Xu, W.; Chitnis, P. R.; Valieva, A.; van der Est, A.; Pushkar, Y. N.; Krystyniak, M.; Teutloff, C.; Zech, S. G.; Bittl, R.; Stehlik, D.; Zybailov, B.; Shen, G.; Golbeck, J. H. *J. Biol. Chem.* **2003**, *278*, 27864. Xu, W.; Chitnis, P. R.; Valieva, A.; van der Est, A.; Brettel, K.; Guergova-Kuras, M.; Pushkar, Y. N.; Zech, S. G.; Stehlik, D.; Shen, G.; Zybailov, B.; Golbeck, J. H. *J. Biol. Chem.* **2003**, *278*, 27876.

(22) Becke, A. D. *Phys. Rev. A* **1988,** *38*, 3098.

(23) Perdew, J. P. *Phys. Rev. B* **1986**, *33*, 8822.

(24) Frisch, M. J.; Trucks, G. W.; Schlegel, H. B.; Scuseria, G. E.; Robb, M. A.; Cheeseman, J. R.; Zakrzewski, V. G.; Montgomery, J. A., Jr.; Stratmann, R. E.; Burant, J. C.; Dapprich, S.; Millam, J. M.; Daniels, A. D.; Kudin, K. N.; Strain, M. C.; Farkas, O.; Tomasi, J.; Barone, V.; Cossi, M.; Cammi, R.; Mennucci, B.; Pomelli, C.; Adamo, C.; Clifford, S.; Ochterski, J.; Petersson, G. A.; Ayala, P. Y.; Cui, Q.; Morokuma, K.; Malick, D. K.; Rabuck, A. D.; Raghavachari, K.; Foresman, J. B.; Cioslowski, J.; Ortiz, J. V.; Baboul, A. G.; Stefanov, B. B.; Liu, G.; Liashenko, A.; Piskorz, P.; Komaromi, I.; Gomperts, R.; Martin, R. L.; Fox, D. J.; Keith, T.; Al-Laham, M. A.; Peng, C. Y.; Nanayakkara, A.; Gonzalez, C.; Challacombe, M.; Gill, P. M. W.; Johnson, B.; Chen, W.; Wong, M. W.; Andres, J. L.; Gonzalez, C.; Head-Gordon, M.; Replogle, E. S.; Pople, J. A. *Gaussian 98*, Revisions A.7 and A.9; Gaussian, Inc.: Pittsburgh, PA, 1998.

(25) Bergner, A.; Dolg, M.; Küchle, W.; Stoll, H.; Preuss, H. *Mol. Phys.* **1993,** *80*, 1431. d-Functions were taken from: *Gaussian Basis Sets for Molecular Calculations*; Huzinaga, S., Ed.; Elsevier: New York, 1984.

(26) Godbout, N.; Salahub, D. R.; Andzelm, J.; Wimmer, E. *Can. J. Chem.* **1992,** *70*, 560.

(27) A full optimization of a complex between UQ-EM$^{\bullet-}$ and the SIG fragment provided somewhat different hydrogen bond lengths: 2.26 (Ser L223), 2.03 (Ile L224), and 2.47 Å (Gly L225). However, computed **g**-tensor components for this structure differed by less than 20 ppm.

(28) Salahub, D. R.; Fournier, R.; Mlynarski, P.; Papai, I.; St-Amant, A.; Ushio, J. *Density Functional Methods in Chemistry*; Labanowski, J., Andzelm, J., Eds.; Springer, New York, 1991.

(29) Hess, B. A.; Marian, C. M.; Wahlgren, U.; Gropen, O. *Chem. Phys. Lett.* **1996,** *251*, 365.

(30) Schimmelpfennig, B. 1996 Atomic Spin−Orbit Mean-Field Integral Program, Stockholms Universitet, Stockholm, Sweden.

(31) Kaupp, M.; Reviakine, R.; Malkina, O. L.; Arbuznikov, A.; Schimmelpfennig, B.; Malkin, V. G. *J. Comput. Chem.* **2002**, *23*, 794.

(32) Ciofini, I.; Reviakine, R.; Arbuznikov, A.; Kaupp, M. *Theor. Chem. Acc.* In press.

(33) J. Asher, N. Doltsinis, D. Marx, and M. Kaupp, unpublished results.

(34) Similar results have also been obtained for most other main group radicals (see refs 15 and 31), and also in uncoupled DFT calculations of NMR chemical shifts for main group systems with multiple bonds (cf.: Bühl, M.; Kaupp, M.; Malkin, V. G.; Malkina, O. L. *J. Comput. Chem.* **1999**, *20*, 91, and references therein). The overestimate of the most "paramagnetic" component of the tensors by uncoupled DFT calculations appears in all cases to be related to the fact that these large components tend to be dominated by one specific low-energy excitation in the second-order perturbation expression. As the corresponding energy denominator is underestimated by gradient-corrected functionals, the observed overestimation of the tensor component arises. As the "smaller" components are not so much dependent on one excitation but feature contributions from several couplings with larger energy denominators, they tend to be less sensitive to these deficiencies of the currently available functionals.

(35) Nonella, M. *Photosynth. Res.* **1998**, *55*, 253.

(36) O'Malley, P. J. *Biochim. Biophys. Acta* **1999**, *1411*, 101. Rigby, S. E. J.; Evans, M. C. W.; Heathcote, P. *Biochemistry* **1996**, *35*, 6651. O'Malley, P. J. *Chem. Phys. Lett.* **1998**, *285*, 99. Kamlowski, A.; Altenberg-Greulich, B.; van der Est, A.; Zech, S. G.; Bittl, R.; Fromme, P.; Lubitz, W.; Stehlik, D. *J. Phys. Chem. B* **1998**, *102*, 8278.